https://doi.org/10.5194/hess-2020-255
Preprint. Discussion started: 15 June 2020

Hydrology and Earth System Sciences
Discussions

Triple oxygen isotope systematics of evaporation and mixing processes in a dynamic desert lake system

Claudia Voigt[1], Daniel Herwartz[1], Cristina Dorador[2], Michael Staubwasser[1]

[1]Institute of Geology and Mineralogy, University of Cologne, Zülpicher Str. 49b, 50674 Cologne, Germany
[2]Centro de Biotecnología, Universidad de Antofagasta, Angamos 601, 1270300 Antofagasta, Chile

Correspondence to: Claudia Voigt (c.voigt@uni-koeln.de)

Abstract. Triple oxygen isotope measurements are a novel and promising tool in geochemical and hydrological research. This study investigates the combined hydrogen-deuterium and triple oxygen isotope hydrology at the Salar del Huasco, a highly dynamic salt lake system located on the Altiplano Plateau, N-Chile. The region has a semiarid climate that shows strong seasonal and diurnal variability in relative humidity, temperature, and wind conditions. The Salar del Huasco receives inflow from multiple surface sources and groundwater. Episodic flooding after rare rainfall events imposes seasonal fluctuations of the groundwater table and, thus, the lake level. Applying the Craig and Gordon (C-G) evaporation model for triple oxygen isotope data measured along series of increasingly evaporated lakes and ponds within the salar demonstrates the capability to resolve the individual fundamental hydrologic processes of recharge evaporation, simple (pan) evaporation, and transient mixing with surface and subsurface floodwater. Regarding the stream and spring sources, mixing of different generations of recharge is clearly distinguishable from pre-evaporation of a single recharge event. These processes are not resolvable by δ^2H and $\delta^{18}O$ measurements alone. We also show that accurate monitoring of the isotopic composition of ambient water vapour and an estimate of the wind turbulence coefficient in the C-G model are critical aspects required to quantify the hydrologic balance. The wind turbulence coefficient, here 0.54, may be determined accurately from on-site evaporation experiments by fitting evaporation trajectories to the d-excess, $\delta^{18}O$ and residual fraction data.

1 Introduction

Triple oxygen isotope analysis of ice, lake water, plant water, water structurally bonded in minerals – e.g. gypsum – or minerals exchanging with ambient water during their formation – e.g. amorphous silica and carbonate – have been recognized as a potentially powerful tool in studies of the present and the past hydrologic cycle (e.g. Landais et al., 2006, 2008; Uemura et al., 2010; Surma et al., 2018, 2015; Herwartz et al., 2017; Li et al., 2017; Alexandre et al., 2018, 2019; Evans et al., 2018; Gázquez et al., 2018; Passey and Ji, 2019). The foundations of this tool lie in isotope fractionation theory, which predicts small differences in the relationship between $^{17}\alpha$ and $^{18}\alpha$ during kinetic and equilibrium fractionation (Angert et al., 2004). Later, improvements in analytical procedures (Baker et al., 2002) allowed to resolve these small variations (Barkan and Luz, 2005, 2007). The triple oxygen isotope exponent $\theta = \ln {}^{17}\alpha / \ln {}^{18}\alpha$ was found to be 0.529 for liquid–vapour equilibrium (Barkan and

https://doi.org/10.5194/hess-2020-255
Preprint. Discussion started: 15 June 2020


Hydrology and Earth System Sciences
Discussions

Luz, 2005) and 0.5185 for diffusion of water vapour in air (Barkan and Luz, 2007). Triple oxygen isotope analyses of meteoric water across the globe reveal a curved relationship between $\delta^{17}O$ and $\delta^{18}O$ (Li et al., 2015) defining an average trend line – the Global Meteoric Water Line (GMWL) – similarly to the classic $\delta^{2}H$–$\delta^{18}O$ system (Luz and Barkan, 2010):

$$\delta'^{17}O = 0.528 \cdot \delta'^{18}O + 0.000033 \quad (1)$$

with $\delta'^{x}O = 1000 \cdot \ln(\delta^{x}O/1000 + 1)$. For better visualization of deviations from the GMWL, the ^{17}O-excess parameter has been defined (Luz and Barkan, 2010):

$$^{17}O - \text{excess} = \delta'^{17}O - 0.528 \cdot \delta'^{18}O \quad (2)$$

In natural desert lakes, the progress of evaporation causes a systematic decrease of ^{17}O-excess largely in response to relative humidity. The evaporation trend is principally predictable on regional scale by the classic Craig–Gordon (C-G) isotopic evaporation model (Surma et al., 2015, 2018). The studies by Surma et al. (2015, 2018) also laid out how, besides humidity, other climate variables and hydrological parameters including temperature, wind turbulence, the isotopic composition of atmospheric vapour, continuous groundwater recharge, and progressively increasing salinity shape evaporation trajectories in a diagram of ^{17}O-excess over $\delta^{18}O$.

Most highly evaporative environments show significant seasonal variability in all the above variables. In addition, mixing with episodic sources – e.g. flooding after thunderstorms or snowmelt – or simply a variable proportion of multiple groundwater sources with different composition may affect lake's isotopic composition. To examine these factors, we tested the applicability and robustness of the C–G model for triple oxygen isotopes in a complex and highly dynamic desert lake system – the Salar del Huasco, an endorheic salt flat located on the semiarid high-altitude Altiplano Plateau, N-Chile. The hydrological balance of this salar is controlled by a shallow groundwater table, perennial streams, rare and highly seasonal precipitation, and episodic injection of runoff water after heavy rainfalls or snowmelt. The environment is characterized by exceptionally high evaporation rates and high variability in relative humidity and temperature throughout the year with considerable diurnal amplitude. An on-site weather station provides records of local weather data. In addition, we were able to constrain relevant variables from the C–G model equation by in-situ pan evaporation experiments. Springs around the Salar del Huasco were sampled to evaluate isotopic variability of inflowing water sources. We show evaporation trajectories modelled for seasonal conditions at the Salar del Huasco in comparison to measured isotope data from water samples covering a 300 ‰ salinity range. This study identifies many aspects of the seasonal dynamics in this complex hydrological system that influence the isotopic composition of natural ponds at the Salar del Huasco. We also demonstrate that triple oxygen isotope analyses, in contrast to classic $\delta^{2}H$ and $\delta^{18}O$ measurements, can distinguish different major hydrological processes like recharge and mixing and allow to identify changes in the hydrological balance of lakes.

https://doi.org/10.5194/hess-2020-255
Preprint. Discussion started: 15 June 2020


Hydrology and Earth System Sciences
Discussions

2 Study Area

The Salar del Huasco is an endorheic salt flat located in the south of a longitudinal volcano-tectonic depression at the western margin of the Chilean Altiplano at about 3770 m (Fig. 1). It covers an area of about 50 km² but only 5 % of the surface is permanently covered by water (Risacher et al., 2003).

Mean annual values of relative humidity and temperatures are 42 % and 4°C, respectively (CEAZA, 2019). Both relative humidity and temperature are highly variable throughout the year with mean seasonal values of 59 % and 8°C in austral summer (Dec–Mar) and 34 % and 1°C in austral winter (Jun–Sep) (CEAZA, 2019). Day-night fluctuations range between 1 and 99 %, and from -19°C to 22°C (CEAZA, 2019). Mean annual wind speed is about 2.5 $m \cdot s^{-1}$, most times coming from S to SW direction (CEAZA, 2019). Typically, it is calm in the morning, but very windy in the afternoon with 4 $m \cdot s^{-1}$ average wind speed and gusts up to 20 $m \cdot s^{-1}$ (CEAZA, 2019).

Precipitation occurs mainly in austral summer (Dec–Mar), where it is often of convective nature and related to easterly airflow from the Atlantic Ocean and the Amazon Basin (e.g. Aravena et al., 1999; Garreaud et al., 2003; Houston, 2006). In contrast, less frequent winter rains and snow are associated with the interaction of cold air masses from the Pacific with tropical air masses from the Amazon Basin (Aravena et al., 1999). Long-term mean annual precipitation is 150 $mm \cdot a^{-1}$, but interannual variability is high due to their dependence on wind patterns (Garreaud and Aceituno, 2001; Risacher et al., 2003).

The hydrogeological system of the Salar del Huasco consists of three aquifers, where the upper and the intermediate aquifer are located in the basin's sediment infill, separated by a thin aquitard, and the lower aquifer is formed in volcanic bedrock (Acosta and Custodio, 2008). The upper aquifer is recharged by the Collacagua river that drains the northern part of the basin and completely infiltrates 10 km before reaching the salar (Acosta and Custodio, 2008). In periods of heavy rainfall, the river can directly flow into the salar leading to widespread flooding of the northern area (Fig. 2e). Several springs and creeks around the salar and the shallow groundwater table contribute to the formation of perennial lakes. Furthermore, ephemeral ponds emerge episodically due to precipitation, surface and subsurface runoff and a rising groundwater table in the rainy season.

Variable groundwater and stream sources, episodic precipitation and surface runoff, and ephemeral flooding in austral summer result in a highly dynamic system with strongly fluctuating lake level. Based on satellite images and field observations, six main hydrological subsystems could be identified (Fig. 2). Three springs at the western part of the salt flat and one at the south-eastern margin establish two perennial lake systems – *Laguna Grande* and *Laguna Jasure* (Fig. 2b). A channel originating from the *Laguna Grande* extends along the southern margin of the salt flat. This connection may contribute to flooding of southern areas during lake's high level (Fig. 2e). Lowering of the water table over the dry season may lead to isolation of small lakes at the southern margin of the salar. A further subsystem in the north is probably fed by subsurface inflow of the Collacagua river. The northern area may become widely flooded in austral summer (Fig. 2e) but dries up rapidly after the rainy season (Fig. 2g). The northern subsystem is at least temporarily connected to the south-eastern system as indicated by a small channel observed in satellite images. A minor subsystem in the north-western area seems to be mainly fed by the shallow groundwater table since no surface inflow could be observed during either field campaign. Several chains of lakes and a number

https://doi.org/10.5194/hess-2020-255
Preprint. Discussion started: 15 June 2020


Hydrology and Earth System Sciences
Discussions

of isolated ponds on topographic highs were observed in the north-western subsystem during field campaigns in September 2017 and 2018. In contrast, despite extensive rainfall in February 2019 that flooded much of the salt flat, the north-western area was almost dry in March 2019.

3 Sampling

Pan evaporation experiments with 600 ml, 800 ml, and 1000 ml of fresh water (0.805 $mS \cdot cm^{-1}$) filled in stainless steel evaporation pans (Ø 20 cm) were carried out on site over a period of three days. Samples were taken every day around 18:00 and, additionally, at the third day after 13:00. The pan filled with 600 ml fresh water, dried up before the end of the experiment so that no sample could be taken in the evening of the last day. Air temperature, relative humidity, and wind speed were monitored locally at the experiment using a *Kestrel 5500 weather meter* (Fig. S1). Mean relative humidity and temperature are 4°C and 35 % over the whole period of the experiment. As temperatures dropped below 0°C in the night, a considerable fraction, if not all, of the water in the pans froze during the night leading to either a solid ice block or a thick ice layer above the remaining liquid. Consequently, evaporation from pans was mostly restricted to daytime. The effective evaporation time interval was assumed to last from 9:30 to 23:30 – the period when T > 0°C. During that time, average air temperature and relative humidity were 11°C and 21 % with extreme values of 23°C and 7 % occurring just after midday (Fig. S1). Water temperatures measured during sampling were found to be up to 5°C lower than ambient air temperatures. However, during midday, temperatures of water may exceed air temperatures by several degrees due to solar heating of the pans. The wind was very strong between 12:00 and 19:00 with an average wind speed of 5 $m \cdot s^{-1}$ and gusts up to 14 $m \cdot s^{-1}$ coming from S to W direction, i.e. the general direction of the Pacific coast.

Natural water samples from the Salar del Huasco were taken during field campaigns in September 2017, September 2018, and March 2019 (Fig. 2 and Table S1). The sample set includes springs, perennial lakes (*Laguna Grande* in the W, and *Laguna Jasure* in the SE) and ephemeral ponds of which several were apparently recharged and some apparently stagnant. Lakes and ponds are all very shallow (5–30 cm). Samples were taken from the water surface and temperature, pH, and conductivity were measured on site using a digital precision meter *Multi 3620 IDS*.

In the south-eastern area, a perennial spring fed a chain of lakes with generally low salinity < 2 $g \cdot l^{-1}$. Some ponds were visibly connected by streams and creeks. Others located closer to the eastern margin of the salt flat, were topographically elevated and therefore isolated from the main south-eastern inflow. Satellite images indicate that ponds closer to the salar's centre may represent a mixture of source water from the south-eastern inflow and the northern Collacagua subsystem (Fig. 2e).

Ponds from the northern area sampled in 09/17 were characterized by an extreme salinity gradient from 2 to 343 $g \cdot l^{-1}$, broadly decreasing from east to west (Table S1). These ponds were often salt-encrusted and showed black, sulphur-reducing microbial mats at the bottom. In 03/19, this entire area was covered by a large low-salinity lake.

In the north-western area, a spring originating from a small vegetated hill fed a series of ponds with salinities < 1 $g \cdot l^{-1}$. An adjacent chain of ponds sampled in 09/17 about 750 m to the south-east with salinities between 1 and 6 $g \cdot l^{-1}$ was not visibly

https://doi.org/10.5194/hess-2020-255
Preprint. Discussion started: 15 June 2020


Hydrology and Earth System Sciences
Discussions

connected to this spring and must have been sustained by the shallow groundwater table. Three topographically elevated ponds close to the margin had higher salinity of 8 to 40 $g \cdot l^{-1}$. The area around these ponds was more vegetated, indicating that these ponds were older, i.e. represented an earlier flooding but became isolated from recharge.

Additional samples were taken from shallow lakes and ponds at the south to south-western margin of the salar. Satellite images and field observations indicate that this area is flooded by branches of the Laguna Grande during the rainy season and that lowering of the water table over the course of the year leads to isolation of ponds (Fig. 2e and g).

Besides water samples from surface waters, we sampled atmospheric vapour using a Stirling cooler cycle system (*Le-Tehnika*, Kranj, Slovenia) built after Peters and Yakir (2010). Sampling was carried out on the 20.09.17 and the 21.09.17 during the evening from about 18:00 to 21:00 using an air-flow rate of 600–800 $ml \cdot min^{-1}$.

4 Methods

The hydrogen and triple oxygen isotope composition of water samples were analysed by isotope ratio mass spectrometry (IRMS). Complementary concentration data of Na^+, K^+, Ca^{2+}, Mg^{2+}, Cl^-, and SO_4^{2-} in natural samples were determined by ICP-OES (see Fig. S6 and Table S1).

Hydrogen isotope ratios are measured by continuous-flow IRMS of H_2. Water samples are injected in a silicon carbide reactor (*Heka-Tech*, Wegberg, Germany) that is filled with glassy carbon and heated to 1550°C, where they are reduced to H_2 and CO. The produced gases are separated in a helium gas stream (100–130 $ml \cdot min^{-1}$) by gas chromatography (GC) and finally, are introduced in a *Thermo Scientific MAT 253* mass spectrometer for hydrogen isotope analysis. The long-term external reproducibility (SD) is about 0.9 ‰ and 1.15 ‰ for δ^2H and d-excess, respectively.

For triple oxygen isotope analysis, water samples are fluorinated, followed by dual-inlet IRMS of O_2. The method is described in detail in Surma et al. (2015) and Herwartz et al. (2017). In brief, 2.8 µl of water are injected in a heated CoF_3 reactor (370°C) that is continuously flushed with helium (30 $ml \cdot min^{-1}$). The produced oxygen gas is cryogenically purified and trapped in one of twelve sample tubes of a manifold. The manifold is connected to a *Thermo Scientific MAT 253* for dual-inlet IRMS analysis. The long-term external reproducibility (SD) is about 0.12 ‰, 0.25 ‰ and 8 per meg for $\delta^{17}O$, $\delta^{18}O$ and ^{17}O-excess, respectively. All isotope data herein are reported on SMOW–SLAP scale (Schoenemann et al., 2013). The scale is usually contracted using the setup described herein. This can partly be attributed to blank contribution (Herwartz et al., 2017). We observe an increase in scale contraction over the usage period of a CoF_3 reactor filling and a reduction of precision and accuracy of isotopic data, which may indicate that the blank contribution increases with time. To account for this effect, SMOW–SLAP scaling was performed daily using internal standards. Isotope measurements with anomalous high scaling factors or standard deviations were discarded.

https://doi.org/10.5194/hess-2020-255
Preprint. Discussion started: 15 June 2020


Hydrology and Earth System Sciences
Discussions

5 The Craig–Gordon isotopic evaporation model at the Salar del Huasco

The classic evaporation theory distinguishes two principal evaporation scenarios, one with recharge (recharge evaporation) and one without recharge (simple evaporation) (Craig and Gordon, 1965; Criss, 1999; Horita et al., 2008). The C–G model does not account for mixing processes, e.g. as a result of flooding or snowmelt, but can be used to calculate such effect applying mass balance. The three trajectories are principally resolvable in triple oxygen isotope space, whereas in δ^2H–$\delta^{18}O$ space they tend to merge within data uncertainty (Fig. 3). All three trajectories can be expected in a dynamic arid hydrological setting such as the Salar del Huasco. Water affected exclusively by evaporation must progress along either of the two principal evaporation trajectories defined by the C–G model. Episodic flooding after rainfall events are detectable on satellite images of Salar del Huasco (Fig. 2). Thus, mixing processes are likely, but should only be transient due to the rarity of flooding events.

The major variables determining the isotopic composition of evaporating water (i.e. residual water) are relative humidity (h), temperature (T) and wind-induced turbulence (an empirically determined coefficient n) along with the isotopic composition of ambient atmospheric vapour (δ_V), and initial or inflowing water (δ_{WI}) (Craig and Gordon, 1965; Criss, 1999; Horita et al., 2008). The effect of wind turbulence – which is related to wind speed – is accounted for by inserting a correcting exponent to the diffusive fractionation factor, $\alpha_{diff,l-v}^{n}$ (Dongmann et al., 1974). The turbulence coefficient n can theoretically vary between 0 (fully turbulent atmosphere) and 1 (calm atmosphere), but typically assumes values of $n \geq 0.5$ under natural conditions (Gonfiantini, 1986; Mathieu and Bariac, 1996; Surma et al., 2018). Salinity affects isotope activities and increases fluid viscosity thereby decreasing the vapour pressure above the water body. In the C-G model, this may be accounted for by correcting equilibrium fractionation factors for the classic salt effect (Horita, 1989, 2005; Horita et al., 1993) and using effective rather than actual relative humidity. However, this effect only requires consideration in the δ^2H–$\delta^{18}O$ system at salinities > 100 $g \cdot l^{-1}$ and was therefore neglected in our model calculations (Sofer and Gat, 1972, 1975; Horita, 1989, 2005).

The relative isotopic difference between inflowing water (δ_{WI}) and atmospheric vapour (δ_V) mainly determines the resolution of evaporation trajectories for different relative humidity in the triple oxygen isotope plot (Surma et al., 2018). For the given boundary conditions at the Salar del Huasco, evaporation trajectories show low sensitivity to changes in relative humidity, temperature, and the turbulence coefficient in the diagram of ^{17}O-excess over $\delta^{18}O$ (Fig. 4). Thus, seasonal and diurnal variability in these climate variables should have a low impact on the triple oxygen isotope composition of lakes and ponds at the Salar del Huasco supporting the purpose of this study to resolve different hydrological processes of evaporation, recharge, and mixing.

In this study, four of the five variables in the C–G equation are known from monitoring (T, h) and direct measurements (δ_{WI}, δ_V). The turbulence coefficient n is not easily obtainable from wind speed monitoring but can be accurately derived from the evaporation experiment (see Section 6.2). The vapour composition (δ_V) was measured directly but could be more variable over the sampling period than our two days of measurement suggest. There may only be a weak relationship on average between vapour and rainfall composition at the Salar del Huasco. High-precipitation events in austral summer show significant isotopic variability that is related to a variable continental effect in the Amazon Basin and the intensity of convective storms (Aravena

https://doi.org/10.5194/hess-2020-255
Preprint. Discussion started: 15 June 2020


Hydrology and Earth System Sciences
Discussions

et al., 1999). Winter rains comprise generally higher $\delta^{18}O$ values and are isotopically less variable than summer rains. This may be attributed to less variability in the contribution of pre-evaporated water from the Amazon Basin in the dry season and the non-convective nature of winter storms (Aravena et al., 1999). The isotopic composition of winter rains reflects a mixture of moisture from air masses originating from the Amazon Basin and from the Pacific Ocean, while the mean annual isotopic composition of atmospheric vapour over the Salar del Huasco basin is dominated by air masses derived from Pacific sources (Garreaud et al., 2003).

6 Results and discussion

6.1 Atmospheric vapour

Atmospheric vapour was sampled on 20.09.17 and 21.09.17. Measurements revealed an average $\delta^{18}O_V$ of -19.4 ± 2.3 ‰. Average d-excess$_V$ and ^{17}O-excess$_V$ values are 30 ± 3 ‰ and 18 ± 2 per meg, respectively. Seven-day air mass back-trajectories calculated using the HYSPLIT model suggest that air masses during vapour sampling were mainly derived from Pacific sources (Fig. S3). A predominantly western origin of vapour is confirmed for the time of our sampling campaign in 09/17 by 7-day air mass back-trajectories calculated for the month prior to sampling using the HYSPLIT Lagrangian model (Fig. 5; Stein et al., 2015).

Results apparently deviate only slightly from the OIPC model's mean annual $\delta^{18}O_V$ value of -21.8 ‰ (Bowen et al., 2005). However, the OIPC model estimate is based on two fundamentally different precipitation processes, where on one hand there is a major contribution of the Amazon moisture source with convective summer rain, high rainout and depletion of heavy isotopes, and on the other hand a relatively enriched winter snow moisture source (cf. Aravena et al., 1999). These two seasonal aspects coincidently combine to an average value that is similar to our measurements. As such, rainfall data available from the global OIPC precipitation database (Bowen et al., 2005) are not reliable in deriving vapour composition in this environment. The isotopic composition of atmospheric vapour is therefore better represented by the small number of direct measurements of water vapour collected during the sampling campaign at a time, where the actual synoptic weather condition during sampling most likely reflects the annual average condition reasonably well.

6.2 Pan evaporation experiments

Evaporation trajectories in the isotope diagrams were modelled for pan evaporation experiments using the simple (pan) C–G model. Here, the isotopic composition of initial water and atmospheric vapour, salinity, temperature, and relative humidity are constrained by direct measurement or monitoring over the period of the experiment (Table 1). The coefficient *n* for wind-induced turbulence is a parametrized value that cannot be directly measured but is well constrainable from isotopic data. An evaporation trajectory for given boundary conditions with a suitable turbulence coefficient *n* may be derived empirically from a plot of d-excess over the fraction of remaining water by determining the best model fit through all experimental data (Fig. 6). In this diagram, the trajectory is predominantly affected by the magnitude of the turbulence coefficient, and only barely

https://doi.org/10.5194/hess-2020-255
Preprint. Discussion started: 15 June 2020


Hydrology and Earth System Sciences
Discussions

sensitive to the other variables of the C–G equation. Notably, this approach is insensitive to our least well constrained variable, $\delta^{18}O_V$ (Fig. 6b). A Monte Carlo error simulation yields n = 0.44. However, turbulence coefficients observed under natural conditions world-wide are typically ≥ 0.5 (Merlivat and Jouzel, 1979; Gonfiantini, 1986; Mathieu and Bariac, 1996; Surma et al., 2018). The above-average turbulence indicated by this low value could reflect excessive evaporation at prevailing up to gale-force winds during midday, and reduced evaporation during the calmer times of the day during the night and in the early morning when the experiment waters were frozen over. Unfortunately, the freezing at night-time introduces a complicating aspect that results in uncontrollable effects on the relationship between d-excess and the fraction of remaining water in this particular experiment. When the ice begins to melt in the morning, a considerable fraction, if not the whole, resulting water film on top of the pan's frozen surface layer may evaporate at the same time. The fraction of total water in the pan would thus be reduced without affecting the isotopic composition of the bulk ice. In our experimental setup, this essentially equals an overestimation of the fraction of water lost during daytime evaporation and would systematically shift the isotopic data above the predicted trajectory in the plot of d-excess vs residual fraction limiting its potential to precisely estimate the turbulence coefficient. Alternatively, the C–G model may be used to derive the turbulence coefficient *n* by fitting the evaporation trajectory through measured isotopic data in a diagram of d-excess over $\delta^{18}O$. This comes with the caveat of considerable sensitivity to the assumed value for $\delta^{18}O_V$. However, at given boundary conditions – including the measured average $\delta^{18}O_V$ = -19.4 ‰ – the best fit is obtained for a value of n = 0.54 (Fig 7a). For n = 0.44 estimate and the given boundary conditions, the data do not fall on the modelled evaporation trajectory (Fig. 7b). To obtain a fit with n = 0.44, $\delta^{18}O_V$ = -28.9 ± 0.25 ‰ must be assumed. Such a value appears unrealistically low in comparison to our measurements as well as to the hypothetical value derived from the OIPC model assuming equilibrium fractionation between vapour and rain ($\delta^{18}O_V$ = -21.8 ‰). Because n = 0.54 derived from the latter approach is in good agreement with the global range of values, and because the freeze-over of the pan experiment may effectively lead to an undesired weighting of the estimate towards the stormy midday in the former approach that is not representative for the majority of unfrozen natural ponds, we tentatively choose to work with the higher value.

In a ^{17}O-excess vs $\delta^{18}O$ diagram, the isotopic data fall below the predicted evaporation trend, regardless which turbulence coefficient is used. In this case, two unresolvable effects may be the reason for the mismatch. Partial melting during the thawing of our experiment in the morning may result in uncontrollable mixing effects that are only observable in a ^{17}O-excess over $\delta^{18}O$ diagram (Fig S4). Furthermore, in evaporation experiments the diurnal variations of temperature and relative humidity, and corresponding changes of the isotopic end point of evaporation lead to a diurnal evolution of the simple (pan) evaporation trajectory (Fig. S5; Surma et al., 2018). Both effects become increasingly important, as the experiment progresses to smaller residual water volumes, consistent with our data. Unfortunately, we were not able to perform the necessary high-resolution sampling of the evaporation experiment to fully resolve these effects and obtain the most accurate average evaporation trajectory.

In conclusion of this experiment, we suggest that the complementary analysis of all water isotopes in evaporation experiments principally allows to determine the turbulence coefficient and to constrain the isotopic composition of ambient vapour with

https://doi.org/10.5194/hess-2020-255
Preprint. Discussion started: 15 June 2020


Hydrology and Earth System Sciences Discussions

sufficient confidence. The remaining uncertainty in the accuracy of our estimate of *n* in this particular study is, fortunately, not relevant for the following discussion.

6.3 Springs and the Collacagua river

The different aquifers in the Salar del Huasco basin are reasonably similar in isotopic composition as indicated by previously published isotopic data of springs and wells (-12.56 ± 1.36 ‰ in $\delta^{18}O$ and 3.2 ± 5.7 ‰ in d-excess; data from Fritz et al., 1981; Uribe et al., 2015; Jayne et al., 2016). These values are in good agreement with our own data derived from springs sampled in 09/17 around the salar with average $\delta^{18}O$ of -12.45 ± 0.64 ‰, d-excess of 2.2 ± 2.9 ‰, and ^{17}O-excess of 11 ± 7 per meg. The springs' isotopic composition shows only slight intra- and interannual variability comprising average $\delta^{18}O$, d-excess and ^{17}O-excess values of -12.31 ± 0.50 ‰, 1.3 ± 2.2 ‰ and 6 ± 7 per meg in 09/18 and -12.55 ± 0.68 ‰, 5.5 ± 2.0 ‰, and 2 ± 6 per meg in 03/19, respectively. The $\delta^{18}O$ values of springs in the Salar del Huasco basin are within the range of local precipitation ($\delta^{18}O$ = -17 to -13 ‰; Scheihing et al., 2017 and references therein), but the springs' isotopic range generally falls below the GMWL. This seems to be typical for groundwater in the Atacama Desert and other desert environments (Aravena, 1995; Surma et al., 2015, 2018) and may be attributed to evaporation of precipitation during infiltration into the soil (Aravena, 1995). The isotopic compositions of springs from the Salar del Huasco basin plot within the common evaporation trend for the predominant isotopic range of local precipitation in the diagram of d-excess over $\delta^{18}O$ (Fig. 7b). However, in triple oxygen isotope space, the springs' isotopic range falls below the predicted evaporation trend (Fig. 7a). This indicates that groundwater has additionally been modified by mixing processes (Fig. 7). Mixing likely occurs between precipitation and evaporated connate water in the vadose zone during infiltration into the soil and may also take place with water adsorbed onto salts, e.g. halite (NaCl), or structurally bonded water of minerals, e.g. mirabilite ($Na_2SO_4 \cdot 10H_2O$), which were commonly observed in the Salar del Huasco environment.

The Collacagua river that was sampled at about 15 km distance from the salar, revealed similar $\delta^{18}O$ values in 09/18 (-12.38 ‰) and 03/19 (-12.45 ‰) that coincide well with the average isotopic composition of springs. As for the springs, the isotopic composition of the Collacagua river falls below the GMWL comprising d-excess and ^{17}O-excess values of 1.6 ‰ and 5 per meg in 09/18 and 5.8 ‰ and 5 per meg in 03/19, respectively. The Collacagua river and its tributaries originate from springs at different altitudes in the Salar del Huasco basin (c.f. Fig. 1). These springs, and thus the tributaries of the Collacagua river, probably differ slightly in isotopic composition due to the altitude effect (Uribe et al., 2015). The measured isotopic composition of the Collacagua river likely reflects a mixture of water from its tributaries, further modified by evaporation along the riverbed.

6.4 Water isotopes in ponds and lakes in the Salar del Huasco

The isotopic composition of lakes and ponds from the Salar del Huasco sampled in the period from 09/17 to 03/19 principally reflect evaporation trends predicted by the C–G model for given boundary conditions (Table 2; Fig. 9). Most of the ponds fall close to the recharged evaporation trajectory indicating that evaporation along with surface inflow by springs, streams and

https://doi.org/10.5194/hess-2020-255
Preprint. Discussion started: 15 June 2020


Hydrology and Earth System Sciences
Discussions

creeks as well as groundwater recharge dominate the hydrological system (Fig. 9). A few ponds sampled in 03/19 seem to be 'non-recharged' as their isotopic composition follows the simple evaporation trajectory (Fig. 9e). These ponds are probably of transient nature filled up by heavy rainfalls and flooding in 02/19. Both evaporation trends – recharge evaporation and simple (pan) evaporation – are well resolved in a plot of ^{17}O-excess over δ^{18}O but are blurred by insensitivity in a diagram of d-excess over δ^{18}O (Fig. 9).

A considerable number of ponds, particularly those sampled in 09/17, falls below the predicted recharge evaporation trajectory (Fig. 9). This offset may be attributed to uncertainty in the model input parameters (δ_{WI}, δ_V, T, h, n) but can also be related to mixing processes. Both effects are examined in the following.

6.4.1 Model uncertainty

The model input parameters include (1) the isotopic composition of inflowing water (δ_{WI}), which was inferred from the measured isotopic composition of local springs, (2) the isotopic composition of atmospheric vapour (δ_V) estimated from a two-spot measurement, (3) relative humidity (h) and temperature (T), for which mean seasonal daytime conditions were considered, and (4) the turbulence coefficient (n), which was derived from pan evaporation experiments. As previously shown, changes in relative humidity, temperature, and the turbulence coefficient have only a minor impact on evaporation trajectories in triple oxygen isotope space for the given boundary conditions at the Salar del Huasco (Fig. 4). Thus, particularly the uncertainty and variability in the isotopic composition of inflowing water and atmospheric vapour may contribute to deviations and scatter of pond data along the predicted recharge evaporation trajectory in the diagram of ^{17}O-excess over δ^{18}O (Fig. 9a).

Ponds and lakes in the Salar del Huasco receive inflow from multiple sources that especially differ in their ^{17}O-excess values. The isotopic composition of inflowing water also varies slightly intra- and interannually due to the seasonality of precipitation and the impact of evaporation (Fig. 8). The effect of source variability on the evaporation trajectory is illustrated in the figs. 10a and 10b. In these diagrams, evaporation trajectories were modelled for the whole isotopic range of springs observed in 09/17. The variability in the isotopic composition of spring water, particularly in ^{17}O-excess$_{WI}$, broadens the range of evaporation trend lines in the diagram of ^{17}O-excess over δ^{18}O, especially for through-flow lakes (E/I < 0.5). As demonstrated in fig. 10, source variability can account for the offset of most of the ponds. However, a few ponds with apparently high E/I ratios still fall below the predicted envelope (Fig. 10a, b).

The value of $\delta^{18}O_V$ was estimated from a two-spot measurement but the isotopic composition of atmospheric vapour might be more variable over the course of the year. Assuming an uncertainty of 5 ‰ in $\delta^{18}O_V$, the isotopic composition of ponds plotting close to the predicted evaporation trend can be covered (Fig 10c). However, $\delta^{18}O_V$ values of about -30 ‰ or even lower would be necessary to fit the isotopic data with the largest offset (Fig. 10c). This seems to be unlikely considering our measurements (-19.4 ‰). Furthermore, using $\delta^{18}O_V$ = -30.0 ‰, all pond data would fall slightly above the predicted evaporation trajectory in a diagram of d-excess over δ^{18}O (Fig. 10d).

Sensitivity tests suggests that the impact of large seasonal and diurnal variability in relative humidity, temperature, and wind conditions on the isotopic composition of lakes and ponds in the Salar del Huasco is low (Fig. 4). To verify this assumption,

https://doi.org/10.5194/hess-2020-255
Preprint. Discussion started: 15 June 2020


Hydrology and Earth System Sciences
Discussions

we compared recharge evaporation trajectories for mean annual daytime (h = 33 %, T = 8°C) and mean seasonal daytime conditions (h = 6 %, T = 23 %) (Fig. 10e, f). Additionally, we modelled the recharge evaporation trajectories for mean seasonal relative humidity and temperature (h = 17 %, T = 9°C) weighted for the mean diurnal distribution of temperature and wind speed (Fig. 10e, f). High temperature and high wind speed amplify evaporation and were thus stronger weighted. All three evaporation trajectories fall close to each other in triple oxygen isotope space (Fig 10e) demonstrating that variability in relative humidity and temperature cannot account for the deviations of ponds from the recharge evaporation trajectory in the triple oxygen isotope plot. However, the modelled evaporation trajectories cover the whole isotopic range of ponds in the diagram of d-excess over $\delta^{18}O$ (Fig. 10f). Thus, diurnal and seasonal variations in relative humidity, temperature and also wind conditions may contribute to the variability of isotopic data along the recharge evaporation trend line in the plot of d-excess over $\delta^{18}O$.

6.4.2 Mixing within the Salar

The overall uncertainty of model input parameters cannot fully explain the offset of ponds from the predicted recharge evaporation trajectory (Fig. 10). This holds especially for ponds with E/I > 0.5, which are apparently common in the northern area of the salar (Fig. 9a). For these ponds, mixing is certainly an important process.

All ponds and lakes fall within the envelope for mixing defined by the mixing line for a terminal lake (Fig. 9). At the Salar del Huasco, mixing may occur episodically due to fluctuations in the groundwater table that are associated with the seasonality of precipitation and the impact of evaporation. After heavy rainfalls or snowmelt, the groundwater table rises leading to admixture of fresh water to the pre-evaporated shallow subsurface flow or pond water. Mixing is most significant for highly evaporated ponds that isotopically strongly differ from groundwater. Mixing due to episodic flooding occurs only occasionally and, thus, the effect on ponds' isotope composition should be of transient nature. After the mixing event, the isotopic composition of the pond water may tend to re-establish steady-state conditions on the recharge evaporation trajectory. As proposed by Herwartz et al. (2017), mixing processes can also occur continuously by admixture of isotopically light groundwater to a pre-evaporated subsurface flow, leading to variations in the isotopic composition of inflowing water for individual ponds. Continuous mixing may also affect ponds at the Salar del Huasco, additionally to the episodic mixing component.

Besides mixing processes, fluctuations in the groundwater table can lead to changes in the recharge rate, increasing the E/I ratio with decreasing water level. Drop down of the water table over the course of the year may ultimately lead to isolation from recharge for individual ponds. When recharge is completely stopped, the isotopic composition of the lake evolves from the recharge evaporation trajectory towards the simple evaporation trajectory. This is particularly observed in the southern area of the salar, where ponds span a wide range in isotopic composition falling within the envelope spanned by predicted trajectories for recharge and simple (pan) evaporation (Fig. 9).

https://doi.org/10.5194/hess-2020-255
Preprint. Discussion started: 15 June 2020


Hydrology and Earth System Sciences
Discussions

7 Conclusion

The classic Craig-Gordon isotopic evaporation model reliably predicts isotopic evaporation trends of lakes and ponds in highly dynamic lacustrine systems in a desert environment with considerable seasonal and diurnal variability in temperature and relative humidity. The Salar del Huasco is dominated by recharge evaporation. Inflow from multiple sources with some spatial and temporal range in isotopic composition cause minor variability in the isotopic evolution of lakes and ponds along the dominant recharge evaporation trajectory. Deviations from this trajectory occur due to episodic flooding after precipitation events that may result in the emergence of ephemeral non-recharged ponds. Additionally, lateral inflow or a rising groundwater table can cause isotopic mixing of pre-flood brines with slightly pre-evaporated floodwater. It may even be possible to identify unknown sources from such mixing trajectories. A rapidly receding groundwater table over a few months after the flood may lead to cut off from recharge for ephemeral ponds at slightly elevated locations. Our results demonstrate that triple oxygen isotope analyses allow for the identification of these fundamental hydrological processes in the lacustrine environment and in the source region. These processes are not resolvable with conventional δ^2H–$\delta^{18}O$ measurements. To correctly predict evaporation trajectories, knowledge of the vapour composition and the wind turbulence coefficient is critical. The isotopic composition of atmospheric vapour as well as relative humidity and temperature can be reasonably constrained by monitoring, but the turbulence coefficient in the C–G model is a parametrized value that cannot be measured directly. We demonstrated that the turbulence coefficient can be estimated with confidence from a series of in-situ pan evaporation experiments fitting evaporation trajectories to the isotopic data in a plot of d-excess over the fraction of remaining water or in d-excess over $\delta^{18}O$ space. More systematic experimental studies of on-site evaporation may eventually allow to calibrate the turbulence coefficient with respect to wind speed. Monitoring of the triple oxygen isotopic composition is demonstrably a useful tool to investigate and quantify the hydrologic balance of natural water reservoirs in general. This study suggests that the complementary measurement of hydrogen-deuterium and triple oxygen isotopes may significantly improve isotope-hydrologic budgeting of complex water reservoirs in nature.

Data availability

All data reported herein is provided in the Supplement.

Author Contributions

MS, CV and DH designed the study. CV, MS and CD were responsible for field work. CV conducted data analysis. CV, MS and DH evaluated the data. CV, MS and DH wrote the manuscript with contributions from CD.

Competing Interests

The authors declare that they have no conflict of interest.

Acknowledgements

This work was supported by the German Research Foundation (DFG) [268236062 – SFB 1211, subproject D03]. We further thank Franc Megušar and Le-Tehnika (Kranj, Slovenia) for producing the Stirling cooler cycle system.

References

Acosta, O., Custodio, E., 2008. Impactos ambientales de las extracciones de agua subterránea en el Salar del Huasco (norte de Chile). Bol. Geol. y Min. 119, 33–50.

Alexandre, A., Landais, A., Vallet-Coulomb, C., Piel, C., Devidal, S., Pauchet, S., Sonzogni, C., Couapel, M., Pasturel, M., Cornuault, P., Xin, J., Mazur, J.-C., Prié, F., Bentaleb, I., Webb, E., Chalié, F., Roy, J., 2018. The triple oxygen isotope composition of phytoliths as a proxy of continental atmospheric humidity: insights from climate chamber and climate transect calibrations. Biogeosciences 15, 3223–3241.

Alexandre, A., Webb, E., Landais, A., Piel, C., Devidal, S., Sonzogni, C., Couapel, M., Mazur, J., Pierre, M., Prié, F., Vallet-coulomb, C., Outrequin, C., Roy, J., 2019. Effects of leaf length and development stage on the triple oxygen isotope signature of grass leaf water and phytoliths: insights for a proxy of continental atmospheric humidity. Biogeosciences 16, 4613–4625. https://doi.org/10.5194/bg-16-4613-2019

Angert, A., Cappa, C.D., DePaolo, D.J., 2004. Kinetic ^{17}O effects in the hydrologic cycle: Indirect evidence and implications. Geochim. Cosmochim. Acta 68, 3487–3495. https://doi.org/10.1016/j.gca.2004.02.010

Aravena, R., 1995. Isotope hydrology and geochemistry of northern Chile groundwaters. Bull. l'Institut Fr. d'études Andin. 24, 495–503.

Aravena, R., Suzuki, O., Peña, H., Pollastri, A., Fuenzalida, H., Grilli, A., 1999. Isotopic composition and origin of the precipitation in Northern Chile. Appl. Geochemistry 14, 411–422. https://doi.org/10.1016/S0883-2927(98)00067-5

Baker, L., Franchi, I.A., Maynard, J., Wright, I.P., Pillinger, C.T., 2002. A Technique for the Determination of $^{18}O/^{16}O$ and $^{17}O/^{16}O$ Isotopic Ratios in Water from Small Liquid and Solid Samples. Anal. Chem. 74, 1665–1673. https://doi.org/10.1021/ac010509s

Barkan, E., Luz, B., 2005. High precision measurements of $^{17}O/^{16}O$ and $^{18}O/^{16}O$ ratios in H_2O. Rapid Commun. Mass Spectrom. 19, 3737–3742. https://doi.org/10.1002/rcm.2250

Barkan, E., Luz, B., 2007. Diffusivity fractionations of $H_2{}^{16}O/H_2{}^{17}O$ and $H_2{}^{16}O/H_2{}^{18}O$ in air and their implications for isotope hydrology. Rapid Commun. Mass Spectrom. 21, 2999–3005. https://doi.org/10.1002/rcm.3180

Boschetti, T., Cifuentes, J., Iacumin, P., Selmo, E., 2019. Local meteoric water line of northern Chile (18°S-30°S): An

application of error-in-variables regression to the oxygen and hydrogen stable isotope ratio of precipitation. Water 11, 1–16. https://doi.org/10.3390/w11040791

Bowen, G.J., Wassenaar, L.I., Hobson, K.A., 2005. Global application of stable hydrogen and oxygen isotopes to wildlife forensics. Oecologia 143, 337–348. https://doi.org/10.1007/s00442-004-1813-y

CEAZA, (Centro de Estudios Avanzados en Zonas Áridas), 2019. Estación Salar de Huasco [WWW Document]. URL http://www.ceazamet.cl (accessed 11.6.18).

Craig, H., Gordon, L.I., 1965. Deuterium and oxygen 18 variations in the ocean and the marine atmosphere, in: Stable Isotopes in Oceanographic Studies and Paleotemperatures. pp. 9–130.

Criss, R.E., 1999. Principles of Stable Isotope Distribution. Oxford University Press.

Dongmann, G., Nürnberg, H.W., Förstel, H., Wagener, K., 1974. On the enrichment of $H_2{}^{18}O$ in the leaves of transpiring plants. Radiat. Environ. Biophys. 11, 41–52. https://doi.org/10.1007/BF01323099

Evans, N.P., Bauska, T.K., Gázquez-sánchez, F., Brenner, M., Curtis, J.H., Hodell, D.A., 2018. Quantification of drought during the collapse of the classic Maya civilization. Science (80-.). 501, 498–501.

Fritz, P., Suzuki, O., Silva, C., Salati, E., 1981. Isotope hydrology of groundwaters in the Pampa del Tamarugal, Chile. J. Hydrol. 53, 161–184. https://doi.org/10.1016/0022-1694(81)90043-3

Garreaud, R., Vuille, M., Clement, A.C., 2003. The climate of the Altiplano: Observed current conditions and mechanisms of past changes. Palaeogeogr. Palaeoclimatol. Palaeoecol. 194, 5–22. https://doi.org/10.1016/S0031-0182(03)00269-4

Garreaud, R.D., Aceituno, P., 2001. Interannual Rainfall Variability over the South American Altiplano. J. Clim. 14, 2779–2789. https://doi.org/10.1175/1520-0442(2001)014<2779:IRVOTS>2.0.CO;2

Gázquez, F., Morellón, M., Bauska, T., Herwartz, D., Surma, J., Moreno, A., Staubwasser, M., Valero-Garcés, B., Delgado-Huertas, A., Hodell, D.A., 2018. Triple oxygen and hydrogen isotopes of gypsum hydration water for quantitative paleo-humidity reconstruction. Earth Planet. Sci. Lett. 481, 177–188. https://doi.org/10.1016/j.epsl.2017.10.020

Gonfiantini, R., 1986. Environmental isotopes in lake studies, in: Fontes, D., Fritz, P. (Eds.), Handbook of Environmental Isotope Geochemistry. Elsevier Science, pp. 119–168.

Haese, B., Werner, M., Lohmann, G., 2013. Stable water isotopes in the coupled atmosphere – land surface model ECHAM5-JSBACH. Geosci. Model Dev. 6, 1463–1480. https://doi.org/10.5194/gmd-6-1463-2013

Herwartz, D., Surma, J., Voigt, C., Assonov, S., Staubwasser, M., 2017. Triple oxygen isotope systematics of structurally bonded water in gypsum. Geochim. Cosmochim. Acta 209, 254–266. https://doi.org/10.1016/j.gca.2017.04.026

Horita, J., 1989. Stable isotope fractionation factors of water in hydrated saline mineral-brine systems. Earth Planet. Sci. Lett. 95, 173–179. https://doi.org/10.1016/0012-821X(89)90175-1

Horita, J., 2005. Saline waters, in: Aggarwal, P.K., Gat, J.R., Froehlich, K.F.O. (Eds.), Isotopes in the Water Cycle: , Present and Past Future of a Developing Science. IEA, pp. 271–287.

Horita, J., Cole, D.R., Wesolowski, D.J., 1993. The activity-composition relationship of oxygen and hydrogen isotopes in aqueous salt solutions: II. Vapor-liquid water equilibration of mixed salt solutions from 50 to 100°C and geochemical

https://doi.org/10.5194/hess-2020-255
Preprint. Discussion started: 15 June 2020


Hydrology and Earth System Sciences
Discussions

implications. Geochim. Cosmochim. Acta 57, 4703–4711.

Horita, J., Rozanski, K., Cohen, S., 2008. Isotope effects in the evaporation of water: a status report of the Craig-Gordon model. Isotopes Environ. Health Stud. 44, 23–49. https://doi.org/10.1080/10256010801887174

Houston, J., 2006. Variability of precipitation in the Atacama Desert: Its causes and hydrological impact. Int. J. Climatol. 26, 2181–2198.

Jayne, R.S., Pollyea, R.M., Dodd, J.P., Olson, E.J., Swanson, S.K., 2016. Spatial and temporal constraints on regional-scale groundwater flow in the Pampa del Tamarugal Basin, Atacama Desert, Chile. Hydrogeol. J. 24, 1921–1937. https://doi.org/10.1007/s10040-016-1454-3

Landais, A., Barkan, E., Luz, B., 2008. Record of $\delta^{18}O$ and ^{17}O-excess in ice from Vostok Antarctica during the last 150,000 years. Geophys. Res. Lett. 35, 1–5. https://doi.org/10.1029/2007GL032096

Landais, A., Barkan, E., Yakir, D., Luz, B., 2006. The triple isotopic composition of oxygen in leaf water. Geochim. Cosmochim. Acta 70, 4105–4115. https://doi.org/10.1016/j.gca.2006.06.1545

Li, S., Levin, N.E., Soderberg, K., Dennis, K.J., Caylor, K.K., 2017. Triple oxygen isotope composition of leaf waters in Mpala, central Kenya. Earth Planet. Sci. Lett. 468, 38–50. https://doi.org/10.1016/j.epsl.2017.02.015

Luz, B., Barkan, E., 2010. Variations of $^{17}O/^{16}O$ and $^{18}O/^{16}O$ in meteoric waters. Geochim. Cosmochim. Acta 74, 6276–6286. https://doi.org/10.1016/j.gca.2010.08.016

Mathieu, R., Bariac, T., 1996. A numerical model for the simulation of stable isotope profiles in drying soils. J. Geophys. Res. Atmos. 101, 12685–12696. https://doi.org/10.1029/96JD00223

Merlivat, L., Jouzel, J., 1979. Global climatic interpretation of the deuterium-oxygen 18 relationship for precipitation. J. Geophys. Res. 84, 5029–5033. https://doi.org/10.1029/JC084iC08p05029

Passey, B.H., Ji, H., 2019. Triple oxygen isotope signatures of evaporation in lake waters and carbonates: A case study from the western United States. Earth Planet. Sci. Lett. 518, 1–12. https://doi.org/10.1016/j.epsl.2019.04.026

Peters, L.I., Yakir, D., 2010. A rapid method for the sampling of atmospheric water vapour for isotopic analysis. Rapid Commun. Mass Spectrom. 24, 103–108. https://doi.org/10.1002/rcm.4359

Risacher, F., Alonso, H., Salazar, C., 2003. The origin of brines and salts in Chilean salars: A hydrochemical review. Earth-Science Rev. 63, 249–293. https://doi.org/10.1016/S0012-8252(03)00037-0

Scheihing, K., Moya, C., Struck, U., Lictevout, E., Tröger, U., 2017. Reassessing Hydrological Processes That Control Stable Isotope Tracers in Groundwater of the Atacama Desert (Northern Chile). Hydrology 5, 1–22. https://doi.org/10.3390/hydrology5010003

Schoenemann, S.W., Schauer, A.J., Steig, E.J., 2013. Measurement of SLAP2 and GISP $\delta^{17}O$ and proposed VSMOW-SLAP normalization for $\delta^{17}O$ and $^{17}O_{excess}$. Rapid Commun. Mass Spectrom. 27, 582–590. https://doi.org/10.1002/rcm.6486

Sofer, Z., Gat, J.R., 1972. Activities and concentrations of oxygen-18 in concentrated aqueous salt solutions: Analytical and geophysical implications. Earth Planet. Sci. Lett. 15, 232–238. https://doi.org/10.1016/0012-821X(72)90168-9

Sofer, Z., Gat, J.R., 1975. The isotope composition of evaporating brines: Effect of the isotopic activity ratio in saline solutions.

https://doi.org/10.5194/hess-2020-255
Preprint. Discussion started: 15 June 2020

Earth Planet. Sci. Lett. 26, 179–186. https://doi.org/10.1016/0012-821X(75)90085-0

Stein, A.F., Draxler, R.R., Rolph, G.D., Stunder, B.J.B., Cohen, M.D., Ngan, F., 2015. NOAA's HYSPLIT atmospheric transport and dispersion modeling system. Bull. Am. Meteorol. Soc. 96, 2059–2077. https://doi.org/10.1175/BAMS-D-14-00110.1

Surma, J., Assonov, S., Bolourchi, M.J., Staubwasser, M., 2015. Triple oxygen isotope signatures in evaporated water bodies from the Sistan Oasis, Iran. Geophys. Res. Lett. 42, 8456–8462. https://doi.org/10.1002/2015GL066475

Surma, J., Assonov, S., Herwartz, D., Voigt, C., Staubwasser, M., 2018. The evolution of ^{17}O-excess in surface water of the arid environment during recharge and evaporation. Sci. Rep. 8, 1–10. https://doi.org/10.1038/s41598-018-23151-6

Uemura, R., Barkan, E., Abe, O., Luz, B., 2010. Triple isotope composition of oxygen in atmospheric water vapor. Geophys. Res. Lett. 37, 1–4. https://doi.org/10.1029/2009GL041960

Uribe, J., Muñoz, J.F., Gironás, J., Oyarzún, R., Aguirre, E., Aravena, R., 2015. Assessing groundwater recharge in an Andean closed basin using isotopic characterization and a rainfall-runoff model: Salar del Huasco basin, Chile. Hydrogeol. J. 23, 1535–1551. https://doi.org/10.1007/s10040-016-1383-1

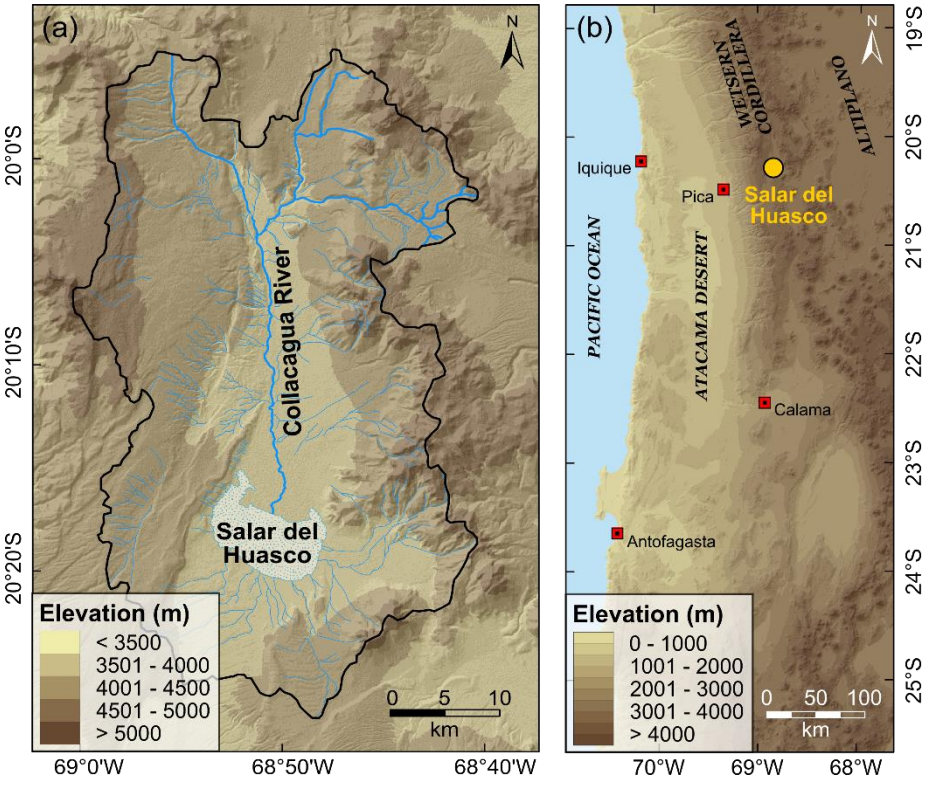

Figure 1: Study Area. (a) Catchment of the Salar del Huasco (Salar del Huasco basin) with drainage. (b) Overview map. (DEM derived from SRTM data, created using ArcGIS 10.5.1)

https://doi.org/10.5194/hess-2020-255
Preprint. Discussion started: 15 June 2020

Hydrology and Earth System Sciences
Discussions
Open Access
EGU

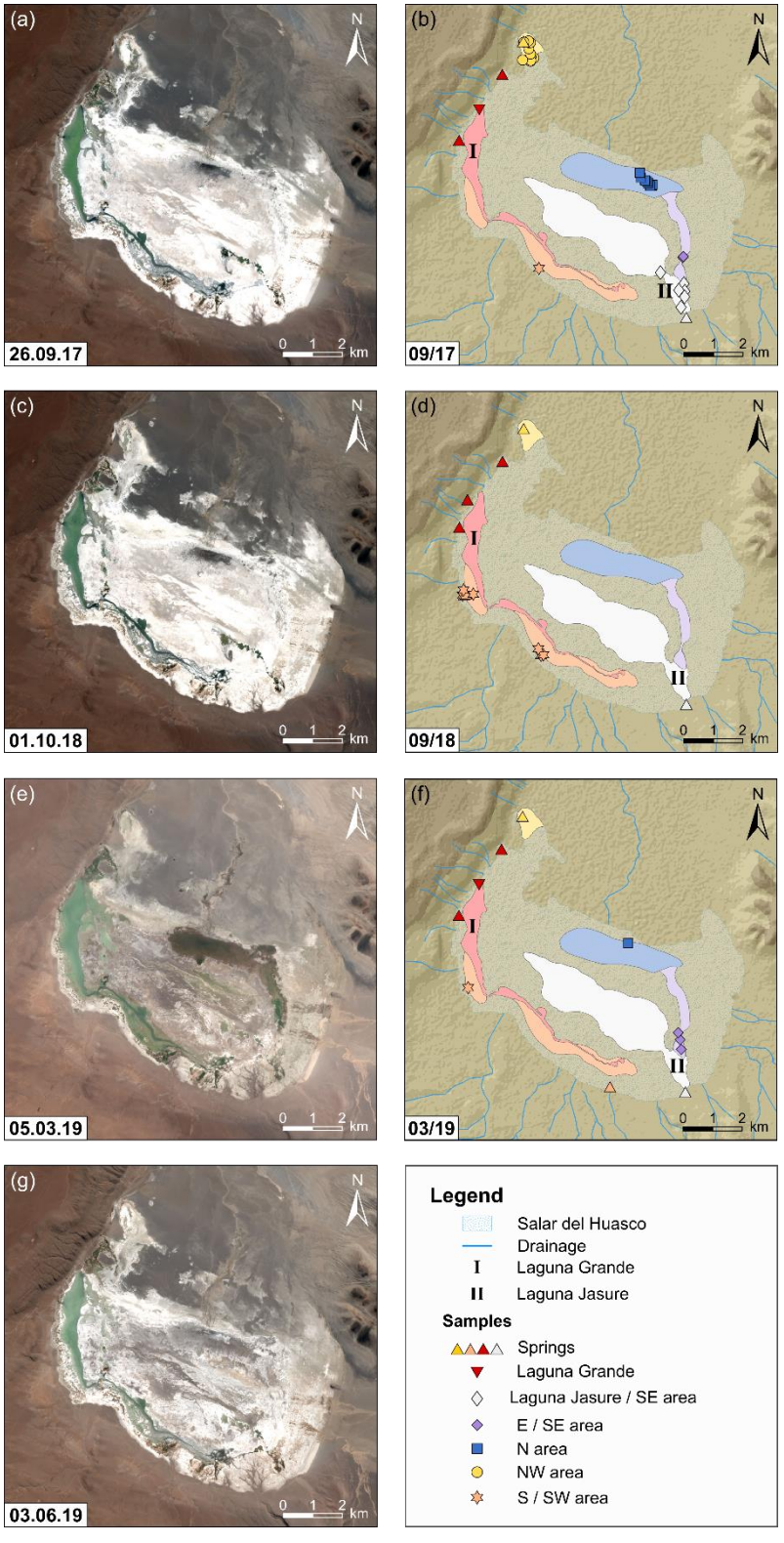

https://doi.org/10.5194/hess-2020-255
Preprint. Discussion started: 15 June 2020

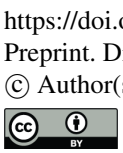

Hydrology and Earth System Sciences
Discussions
Open Access
EGU

Figure 2: Illustration of the hydrological situation at the Salar del Huasco over the sampling period with sample locations for field campaigns in 09/17 ((a) and (b)), 09/18 ((c) and (d)), and 03/19 ((e) and (f)). Panel (g) reflects the hydrological situation at the Salar del Huasco 6 months after the last sampling campaign. Several hydrological subsystems (coloured areas) were identified based on satellite images (Copernicus Sentinel data, 2017, 2018, 2019) and field observations. Different symbols of sample locations refer to the corresponding hydrological subsystem (see text for details). (DEM derived from SRTM data, created using ArcGIS 10.5.1)

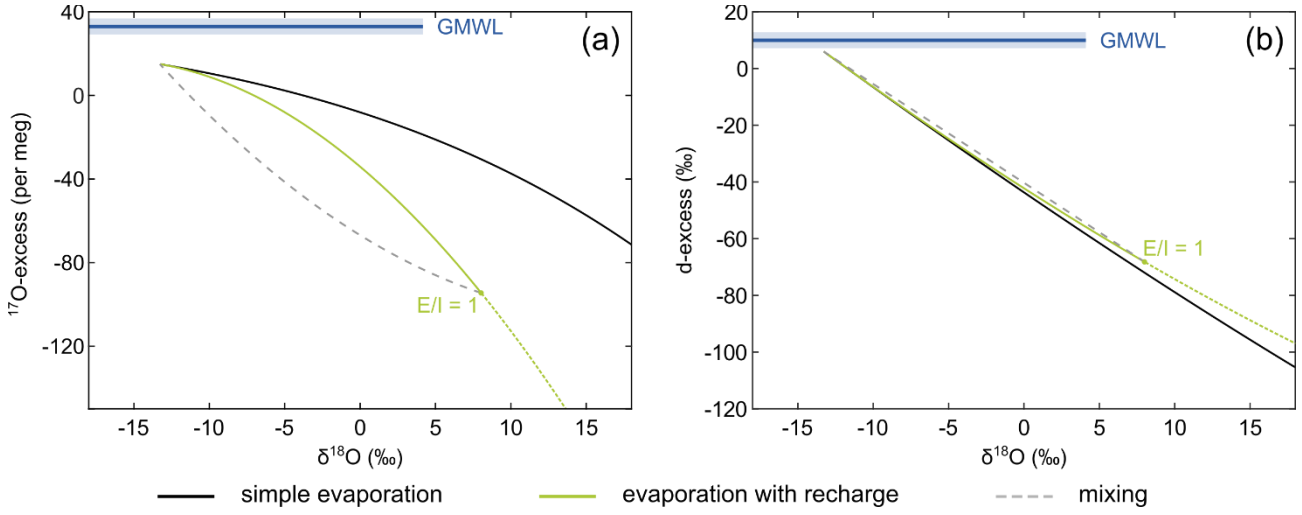

Figure 3: Conceptual comparison of isotope effects associated with the three principal hydrological processes – simple evaporation without recharge, evaporation with recharge, and isotopic mixing – in the diagram of (a) ^{17}O-excess over δ^{18}O and (b) d-excess over δ^{18}O. In the case of simple evaporation, the isotopic composition of an evaporating water body evolves along the black line. Continuous recharge drives the isotopic composition of the evaporating water body below the simple evaporation trajectory onto the green line. The isotopic composition of a recharged lake is determined by the evaporation to inflow (E/I) ratio where increasing E/I lead to higher δ^{18}O and lower ^{17}O-excess values. In the case of a terminal lake (E/I = 1) all inflow is balanced by evaporation. The dashed grey line exemplifies admixture of fresh water similar in isotopic composition to the inflowing water, e.g. flood water, to the evaporated brine of a terminal lake.

https://doi.org/10.5194/hess-2020-255
Preprint. Discussion started: 15 June 2020

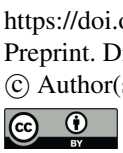

Hydrology and Earth System Sciences
Discussions
Open Access
EGU

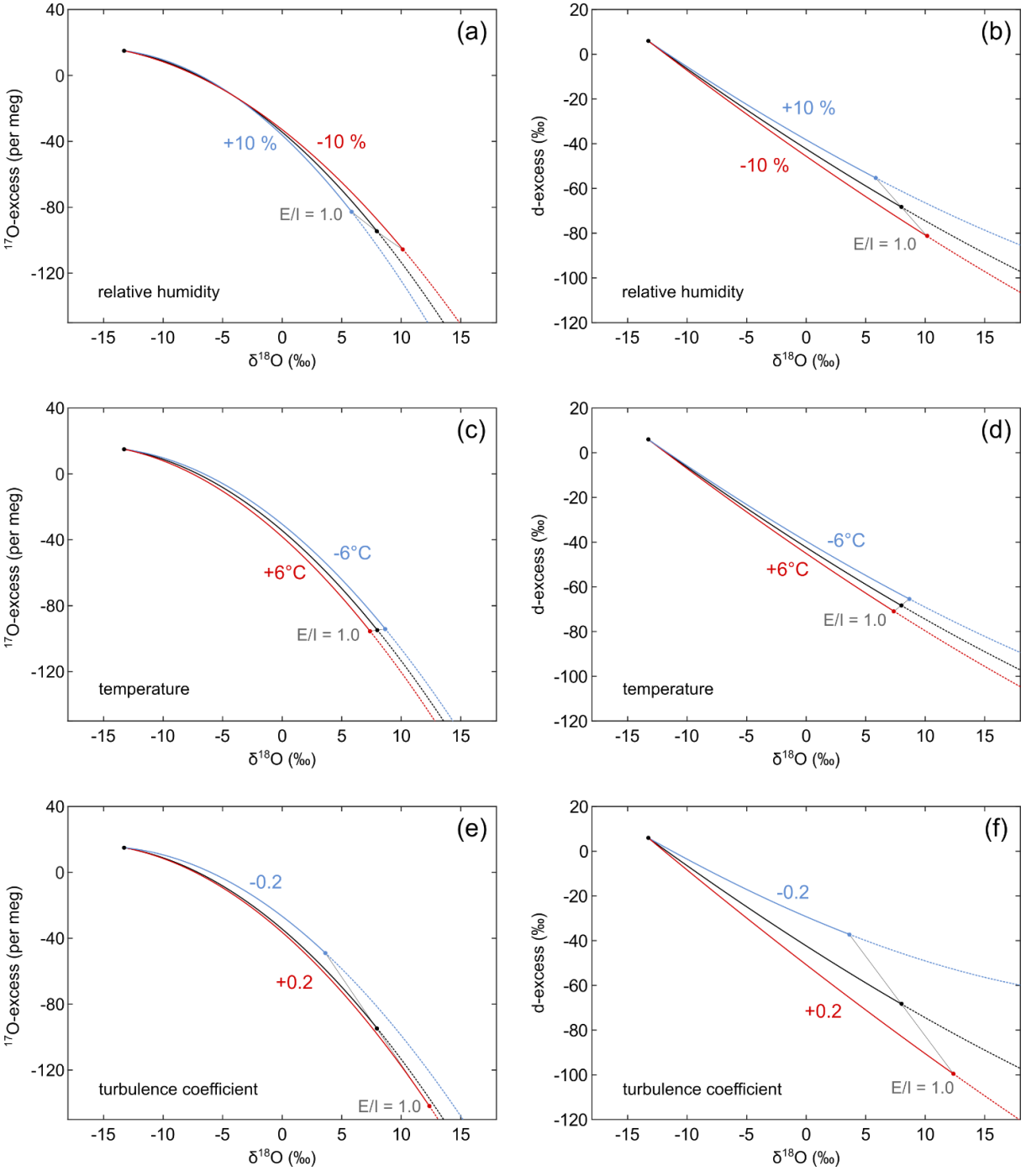

505

Figure 4: Sensitivity of evaporation trajectories in diagrams of ^{17}O-excess over δ^{18}O and d-excess over δ^{18}O to different input parameters for environmental conditions at the Salar del Huasco. Evaporation trajectories have been modelled at variable (a)-(b) relative humidity, (c)-(d) temperature, and (e)-(f) turbulence coefficients. The black line represents the recharge evaporation trajectory modelled for δ^{18}O$_{WI}$ = -13.3 ‰, ^{17}O-excess$_{WI}$ = 15 per meg, d-excess$_{WI}$ = 6 ‰, δ^{18}O$_V$ = -19.4 ‰, ^{17}O-excess$_V$ = 18 per meg,
510 **d-excess$_V$ = 30 ‰, h = 23 %, T = 6°C, n = 0.54.**

https://doi.org/10.5194/hess-2020-255
Preprint. Discussion started: 15 June 2020

Hydrology and Earth System Sciences
Discussions

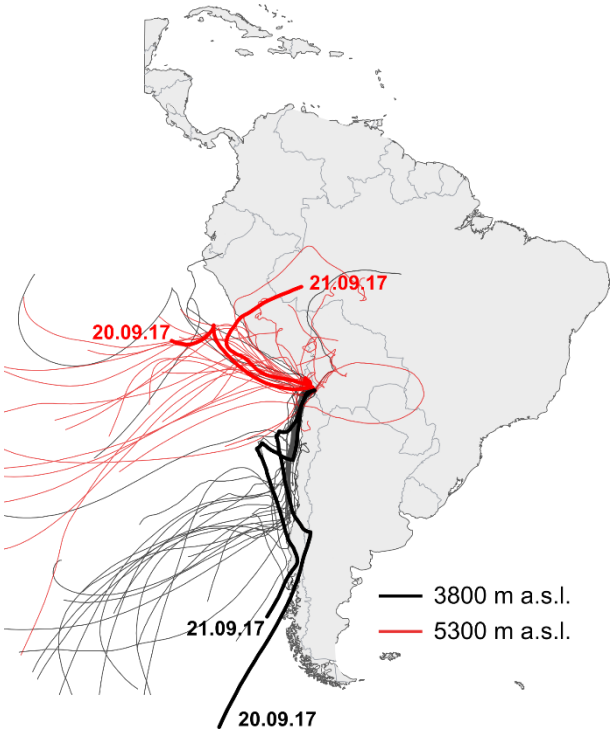

Figure 5: HYSPLIT 7-day air mass back trajectories modelled for ground level at the Salar del Huasco (~3800 m above sea level (a.s.l.)) (black) and 1500 m above ground level (5300 m a.s.l.) (red) in daily resolution for the period from 23.08.2017 to 22.09.2017. The thick red and black trajectories represent the origin of atmospheric air masses at the Salar del Huasco for the time of vapour sampling on 20.09. and 21.09.2017.

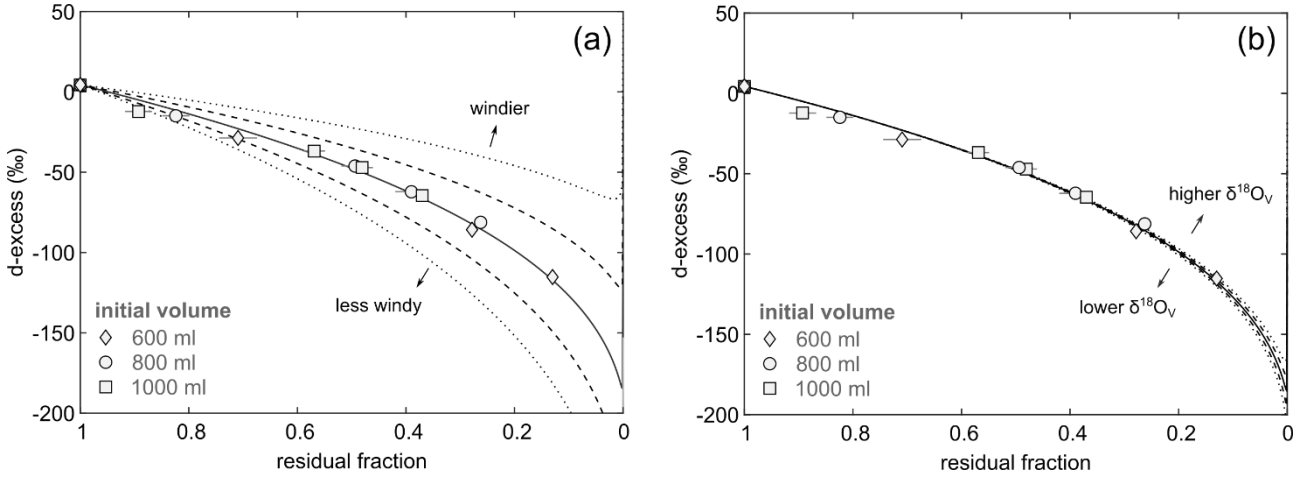

Figure 6: Sensitivity of evaporation trajectories in a plot of d-excess over residual fraction to (a) the turbulence coefficient n and (b) the isotopic composition of atmospheric vapour $\delta^{18}O_V$. Isotopic data of pan evaporation experiments with initial volume of 600 ml (diamonds), 800 ml (circles), 1000 ml (squares) are shown for comparison. Note that the symbol size is in most cases larger than the error bars. The solid line represents the modelled evaporation trajectory for simple evaporation using input parameters as summarized in Table 1 and a turbulence coefficient of 0.44. Dashed lines show model results for (a) different turbulence coefficients

https://doi.org/10.5194/hess-2020-255
Preprint. Discussion started: 15 June 2020

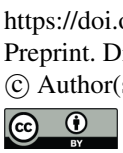

Hydrology and Earth System Sciences
Discussions
Open Access
EGU

in intervals of 0.1 and (b) varying isotopic composition of atmospheric vapour $\delta^{18}O_V$ in intervals of 5 ‰, keeping other parameters constant.

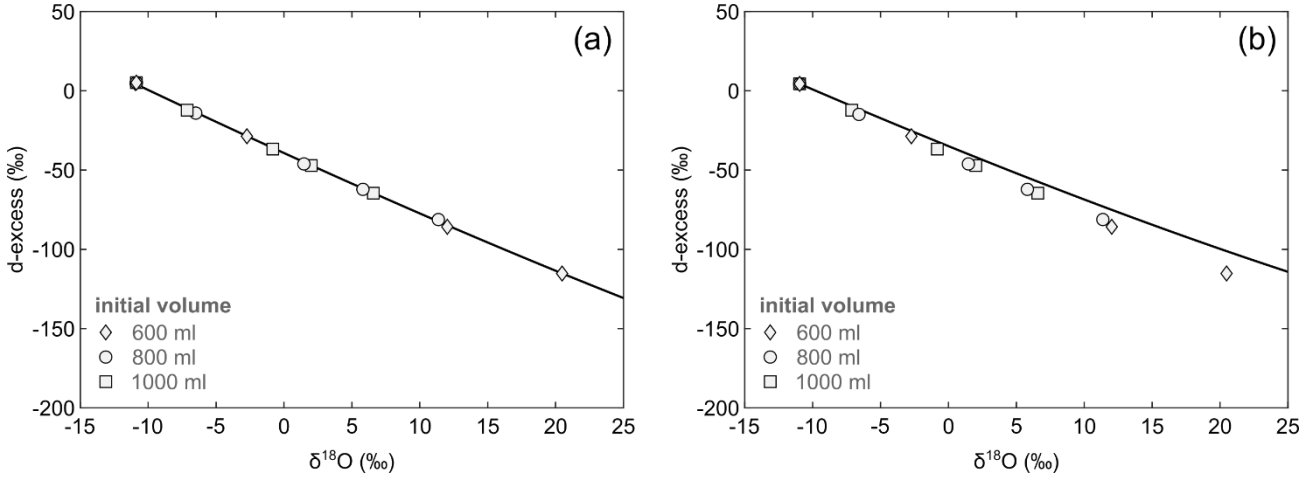

Figure 7: Comparison of simple evaporation trajectories in a diagram of d-excess over $\delta^{18}O$ modelled for (a) n = 0.54 and (b) n = 0.44, keeping other parameters constant (see Table 1). Additionally, isotopic data of pan evaporation experiments with initial volume of 600 ml (diamonds), 800 ml (circles), 1000 ml (squares) are shown. Note that the symbol size is larger than the error bars.

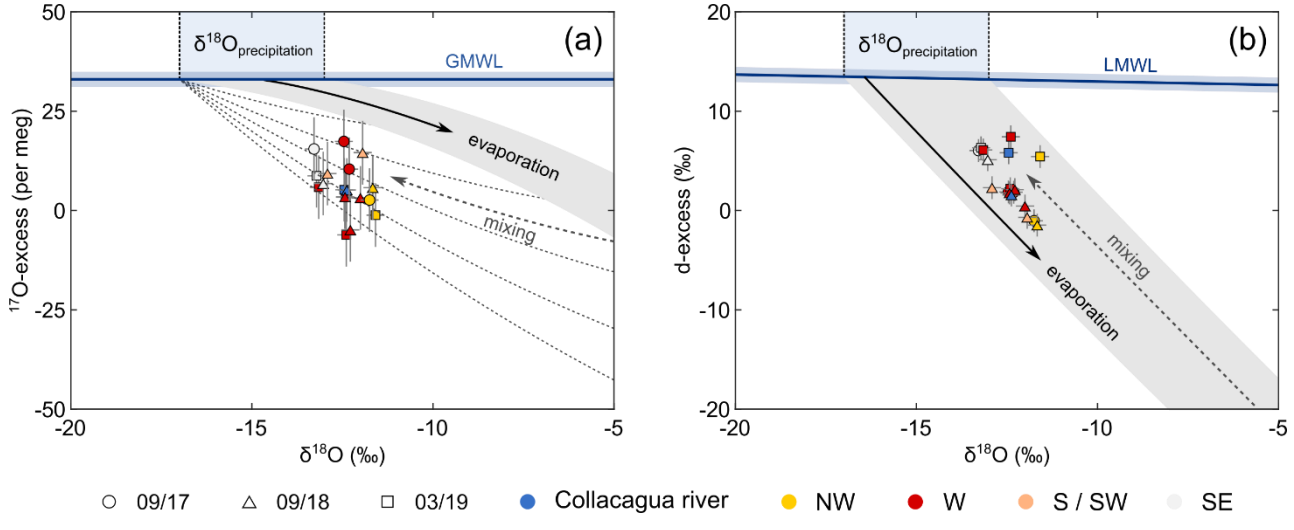

Figure 8: Oxygen (a) and hydrogen (b) isotopic data of the Collacagua river and springs from the Salar del Huasco basin. Colour coding refers to different hydrological subsystems (cf. Fig. 2). The isotopic range of precipitation (-17 to -13 ‰) is derived from previously published data (Scheihing et al., 2017 and references therein). The local meteoric water line (LMWL: $\delta 2H = 7.93 \cdot \delta^{18}O + 12.3$; Boschetti et al., 2019) was derived from precipitation data of northern Chile. Due to the lack of a comprehensive dataset of ^{17}O in precipitation, the global meteoric water line (GMWL) was used as reference in the triple oxygen isotope plot (a). The shaded grey area indicates the isotopic evolution of precipitation undergoing evaporation. The Collacagua river and all local springs fall below the common evaporation trend in a plot of ^{17}O-excess over $\delta^{18}O$ (a). This offset can be explained considering mixing of precipitation with evaporated water in the vadose zone during infiltration into the soil. The effect of mixing is schematically illustrated by the dashed grey lines.

https://doi.org/10.5194/hess-2020-255
Preprint. Discussion started: 15 June 2020

Hydrology and Earth System Sciences
Discussions
Open Access
EGU

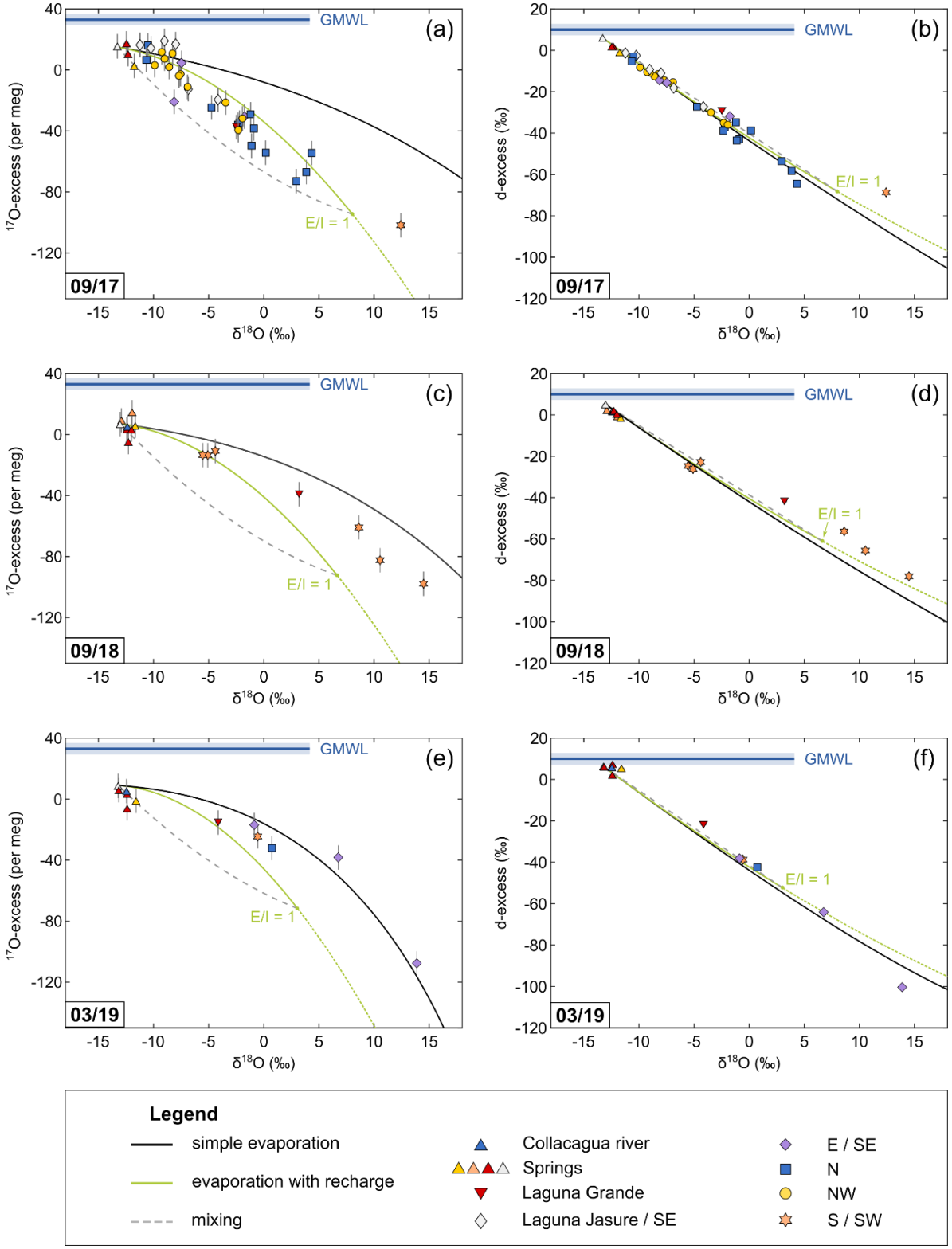

https://doi.org/10.5194/hess-2020-255
Preprint. Discussion started: 15 June 2020

Hydrology and Earth System Sciences
Discussions

Figure 9: Oxygen and hydrogen isotope data of the Collacagua river, springs, lakes and ponds sampled in the Salar del Huasco basin during field campaigns in 09/17 ((a) and (b)), 09/18 ((c) and (d)), and 03/19 ((e) and (f)). Colour coding refers to different hydrological subsystems (see legend and cf. Fig. 2). Note that the symbol size can be larger than the error bars. Trajectories for simple evaporation (black) and evaporation with recharge (green) were modelled using input parameters as summarized in Table 2. Additionally, admixture of fresh groundwater as it might occur during flooding or snowmelt is exemplified for the case of a terminal lake (E/I = 1) (dashed grey line). The Global Meteoric Water Line (GMWL) serves as reference. Note that the apparent lack of samples on a recharge evaporation trajectory in 09/18 and 03/19 is simply the result of a sampling focus on sources and on ponds cut off from recharge during these campaigns.

https://doi.org/10.5194/hess-2020-255
Preprint. Discussion started: 15 June 2020

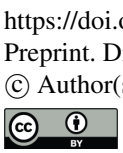

Hydrology and Earth System Sciences
Discussions
Open Access
EGU

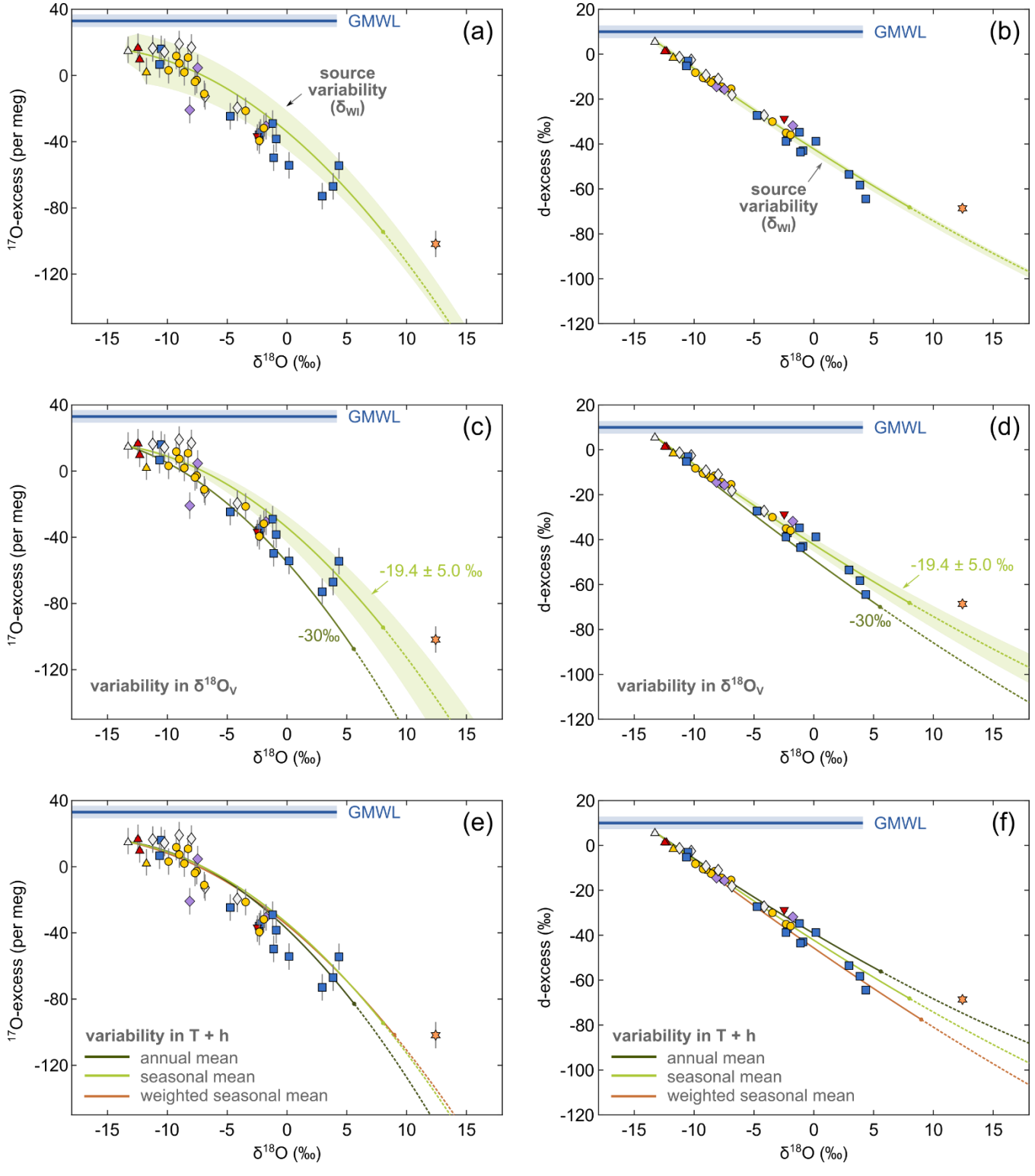

550

https://doi.org/10.5194/hess-2020-255
Preprint. Discussion started: 15 June 2020

Hydrology and Earth System Sciences
Discussions

Figure 10: Uncertainty in model input parameters exemplified for lakes and ponds sampled in 09/17. The green line shows the modelled recharge evaporation trajectory for mean seasonal conditions between 09:00 and 23:00 at the Salar del Huasco. The shaded green areas in panel (a) and (b) illustrate the uncertainty introduced to the modelled trajectory by inflow from multiple springs that slightly differ in isotopic composition (δ_{WI}). Panel (c) and (d) show the effect of variable $\delta^{18}O_V$ on the evaporation trajectory. The shaded green area represents the range of evaporation trajectories for $\delta^{18}O_V$ = -19.4 ± 5.0 ‰. Values of $\delta^{18}O_V$ = -30 ‰ or even lower would be necessary to fit the isotopic data with the largest offset. Panel (e) and (f) illustrate the effect of seasonal and diurnal variability in relative humidity and temperature. Recharge evaporation trajectories have been modelled for (1) annual (Oct–Sep) mean h = 33 % and T = 8°C averaged over the time interval between 9:00 and 23:00 (dark green curve), (2) seasonal (Jun–Sep) mean h = 23 % and T = 6°C in the time interval between 9:00 to 23:00 (light green curve), and (3) seasonal (Jun–Sep) mean h = 17 % and T = 9°C weighted for the average diurnal distribution of temperature and wind speed assuming that high temperature and high wind speed reflect times of high evaporation (brown curve).

https://doi.org/10.5194/hess-2020-255
Preprint. Discussion started: 15 June 2020

Hydrology and Earth System Sciences
Discussions

Table 1: Model input parameters of the simple evaporation model for pan evaporation experiments. The isotopic composition of initial water and atmospheric vapour was determined by measurement. Relative humidity and temperature were monitored over the period of the evaporation experiment. We used mean relative humidity and temperatures values between 9:00 and 23:00 to account for the diurnal variability of the evaporation rate. The turbulence coefficient was derived from pan evaporation experiment data (cf. Section 6.2).

Parameter	Value
$\delta^{18}O_{WI}$ (‰)	-10.96
d-excess$_{WI}$ (‰)	4.4
^{17}O-excess$_{WI}$ (per meg)	16
$\delta^{18}O_{V}$ (‰)	-19.4
d-excess$_{V}$ (‰)	30
^{17}O-excess$_{V}$ (per meg)	18
Temperature (°C)	11
Relative humidity (%)	21
Turbulence coefficient	0.54

Table 2: Model input parameters of the simple and the recharge evaporation model for natural ponds and lakes from the Salar del Huasco. The isotopic composition of inflowing water δ_{WI} was inferred from the spring with the most depleted $\delta^{18}O$ value. The isotopic composition of atmospheric vapour δ_{V} was estimated by direct measurement. For relative humidity and temperature, we assumed mean seasonal values between 9:00 and 23:00 (Jun–Sep for 2017 and 2018, and Dec–Mar for 2019). The value of the turbulence coefficient was derived from pan evaporation experiment data (cf. Section 6.2).

Parameter	2017	2018	2019
$\delta^{18}O_{WI}$ (‰)	-13.28	-13.03	-13.22
d-excess$_{WI}$ (‰)	6.0	5.1	6.3
^{17}O-excess$_{WI}$ (per meg)	15	7	9
$\delta^{18}O_{V}$ (‰)	-19.4	-19.4	-19.4
d-excess$_{V}$ (‰)	30	30	10
^{17}O-excess$_{V}$ (per meg)	18	18	18
Temperature (°C)	6	6	11
Relative humidity (%)	23	30	44
Turbulence coefficient	0.54	0.54	0.54